Diamond & Related Materials 18 (2009) 750–758

Contents lists available at ScienceDirect

Diamond & Related Materials

journal homepage: www.elsevier.com/locate/diamond

The role of inert gas in MW-enhanced plasmas for the deposition of nanocrystalline diamond thin films

O.J.L. Fox [a], J. Ma [a], P.W. May [a,*], M.N.R. Ashfold [a], Yu.A. Mankelevich [b]

[a] School of Chemistry, University of Bristol, Bristol BS8 1TS, UK
[b] Nuclear Physics Institute, Moscow State University, 119991 Moscow, Russia

ARTICLE INFO

Available online 12 January 2009

Keywords:
CVD diamond
Nanocrystalline
Inert gas
Growth

ABSTRACT

Nanocrystalline diamond thin films have been deposited using microwave plasma enhanced deposition with gas mixtures of composition $H_2/CH_4/X$, where X was one of the inert gases He, Ne, Ar and Kr and typically constituted >90% of the total gas flow. The diamond films obtained with each gas mixture deposited at approximately the same rate (0.15–0.5 μm h^{-1}), and all showed similar morphologies and average grain sizes, despite very obvious differences in the appearance and gas temperatures of the respective plasmas. These plasmas were probed by optical emission and cavity ring-down spectroscopy, and results from companion 2D chemical kinetic modelling of the $Ar/H_2/CH_4$ and $He/H_2/CH_4$ plasma were used to guide interpretation of the experimental observations. We conclude that the inert gas, though acting primarily as a buffer, also has significant effects on the thermal conduction of the gas mixtures, the electron temperature and electron energy distribution, and thereby changes the main channels of ionization and input power absorption. As a result, inert gas dilution elevates the electron and gas temperatures, enhances the hydrogen dissociation degree and affects the H/C mixture composition and deposition mechanisms.

© 2009 Elsevier B.V. All rights reserved.

1. Introduction

The production of diamond thin films by chemical vapour deposition (CVD) has become widespread and well studied as a result of the number of promising optical, electronic and mechanical applications that diamond exhibits [1,2]. Research in the late 1980s and early 1990s led to the development of a so-called 'standard growth model' for CVD microcrystalline diamond (MCD) films. This is based on the stepwise abstraction of surface hydrogen atoms by gas phase atomic H, followed by addition of CH_3 radicals, which are considered to be the main growth species in polycrystalline diamond film CVD [3,4]. While the mechanical, thermal and acoustic properties of MCD films have been extensively researched [5], the development of diamond films with smaller crystal size has attracted much recent interest [6]. By changing the plasma conditions, primarily the composition of the gas mixture, it is possible to tune the system to produce different size diamond crystals. A typical gas mixture used for diamond CVD is 1–5% CH_4 in H_2 [1], however, for some plasma systems, a few percent of Ar is often added to help with initiation and stability of the discharge. For example, starting with a set of standard CVD conditions of 90%H_2, 5% CH_4 and 5%Ar used to grow MCD in our plasma reactor, increasing the proportion of CH_4 (*i.e.* the CH_4:H_2 ratio) induces a marked decrease in the average diameter of the diamond crystallites, from a few μm down to 10–100 nm, in a typical mixture of 1%CH_4/2%H_2/Ar. Films with crystallite sizes in the 10s or 100s of nm range are termed nanocrystalline diamond (NCD), and these can exhibit facetted or 'cauliflower-like' morphology depending on the deposition conditions [7]. Films with crystallite sizes <10 nm are sometimes termed ultrananocrystalline diamond (UNCD). The films described in the present paper fall between these two regimes, with crystallite sizes between 10 and 70 nm and, as such, we shall refer to them as (U)NCD.

The majority of research into non-facetted NCD and UNCD growth has been carried out in plasmas with gas mixtures composed of a few percent CH_4 in Ar, sometimes with a few %H_2 included to help stabilise the plasma [6,8,9]. The $Ar/CH_4(/H_2)$ plasmas used to deposit UNCD exhibit a characteristic bright green/white colouration, mainly due to the Swan emission bands of electronically excited C_2 radicals present in the centre of the plasma. This observation led to the original suggestion [10] that the C_2 radical plays an important role in the growth mechanism for UNCD. It was suggested that the concentration of gas phase C_2 could be increased up to the levels necessary to explain the observed UNCD growth rates, if its formation by thermal decomposition of C_2H_2 at the higher gas temperatures was aided by efficient charge exchange from Ar^+ to C_2H_2 or by Penning ionisation from excited metastable Ar*. Either of the latter processes would create $C_2H_2^+$ which could then decompose by dissociative electron-ion recombination to $C_2 + H_2$ [5]. Despite the existence of such routes for converting C_2H_2 into C_2, modelling of the gas phase chemistry (including the Ar^*/C_2H_2 exchange mechanism) by our own group showed that C_2 is not a dominant species close to the substrate surface [11,12], and therefore is unlikely to be responsible for diamond growth.

* Corresponding author.
E-mail address: paul.may@bris.ac.uk (P.W. May).

0925-9635/$ – see front matter © 2009 Elsevier B.V. All rights reserved.
doi:10.1016/j.diamond.2009.01.004

Table 1
Properties of the noble gases [34].

X	1st ionization potential /eV	Atomic mass /(g mol^{-1})	Thermal conductivity* /(mW m^{-1} K^{-1})	Specific heat capacity** /(J mol^{-1} K^{-1})
He	24.48	4.0	141.8	20.8
Ne	21.56	20.2	46.0	20.8
Ar	15.76	39.9	16.9	20.8
Kr	14.00	83.8	8.7	20.8

* measured at 0 °C and 1 atm.
** at 25 °C.

Our group have studied the chemical and physical processes occurring during the deposition of both NCD and UNCD films, and developed a model for growth based on competition for reactive sites by H atoms, CH_3 radicals and other C_1 species [11–13]. The model has recently been refined to be consistent with the experimental observations of all forms of diamond growth, from UNCD to single crystal diamond (SCD) [14,15]. In the model, we conclude that growth of diamond involves a sliding scale, with the different diamond crystallite sizes arising from a smoothly changing ratio of atomic H to C_1 hydrocarbon radicals at the growing surface. The different conditions, gas mixtures, temperatures and pressures reported in the literature for diamond growth simply serve to establish the value of this ratio [H]:[ΣCH_x] (for $x = 1$–3) and with it, the resulting film morphology and growth rate. Experimental evidence for this idea comes from investigations into the role of hydrogen in $H_2/CH_4/Ar$ gas plasmas, which showed that with increasing H_2 the diamond grain size increases with a transition from UNCD to NCD and then to MCD [16,17]. Conversely, if too little hydrogen is present, or the H:C ratio is lowered below ~2 by substituting an equivalent flow rate of C_2H_2 for CH_4, only graphitic films are formed [18].

One way to test the importance of the proposed Ar^+ charge exchange and Ar* Penning reactions is to perform diamond growth using inert gases other than Ar. Rabeau et al. [19] showed that UNCD could also be grown in He/CH_4 plasmas *i.e.* without the need for Ar. Molecular processes in CH_4/H_2 plasmas diluted with Ar and Ne were studied by Tosi et al. [20]. More recently, Griffin and Ray [21] performed a systematic investigation of the role of inert gases by using He, Ne, Ar and Kr based (with CH_4 and H_2) gas mixtures. However, their experiments were performed at pressures of 2.66 mbar (~2 Torr), which is significantly lower than the 100–200 Torr used for most UNCD deposition. They found that while NCD films grown in He, Ne and Ar were very similar, no film was grown in Kr plasmas. They concluded that their results supported the view that C_2 is not necessarily the growth species for UNCD.

The aim of this present work is to perform a similar systematic study of the inert gas based plasmas, $X/CH_4/H_2$, where X = He, Ne, Ar or Kr, but under conditions typically used for deposition of NCD and UNCD. We wish to elucidate the role played by the inert gas (if any) in determining the resulting plasma composition and characteristics, and film growth rates, morphology and crystallite size.

The properties of the four inert gases relevant to these plasmas are given in Table 1. The difference in atomic mass between the inert gas atoms will affect the efficiency of energy and momentum transfer in collisions between them and hydrogen. Helium, having a low mass very similar to that of H (or H_2) will exchange energy and momentum very efficiently upon collision, and thus distribute the power uniformly across the plasma. Alternatively, collisions between Kr (mass 84) and H will be much less efficient, tending to make the plasma more localised and non-uniform. The thermal conductivity of the inert gas controls the efficiency with which heat is spread in the plasma, and will be related to both the efficiency of collisional energy transfer and the mean speed of the atoms. Helium has a very large thermal conductivity, and thus we expect the heat generated at the centre of the plasma to be rapidly distributed into a larger volume — thus producing large, diffuse, but cooler plasmas. Conversely, Kr, with a thermal conductivity 16× lower than that of He should retain the heat in a smaller volume, producing a hot, dense plasma. The ionisation potential (IP) of the noble gases decreases markedly from He to Kr. Gases with lower IP values (Kr and Ar) are expected to readily form secondary plasmas or regions of instabilities around sharp edges or protrusions in the chamber, whereas those with higher IP (He, Ne) values should tend to form stable, controllable plasmas. A combination of the effects of these properties (mass, thermal conductivity and IP) will determine the size, density and stability of the resulting plasma, and these will be investigated in this paper.

2. Experimental

2.1. Deposition conditions

Nanocrystalline diamond thin films were grown by Microwave Plasma Enhanced CVD (MW PECVD) in a 2.45 GHz reactor. The reactor has the general form of a vertically-aligned cylinder of volume ~600 cm^3, with MW power fed from above through a quartz window. The substrates were 1 cm^2 polished single crystal (100) Si, which were seeded with a nanodiamond nucleation layer to initiate film growth. A suspension of 5 nm detonation diamond powder — containing some larger aggregates >100 nm — was prepared using methanol as the liquid medium due to the requirement for high volatility. This colloidal suspension was applied to the Si substrates by one of two techniques. The first method, electrospray, used a 30 kV potential to charge and accelerate the colloidal mixture onto the grounded substrate, whereupon the liquid evaporated leaving the diamond particles uniformly and densely distributed on the surface. The second method involved spin coating the suspension onto the substrate at 4000 rpm. Both seeding methods achieve a high nucleation density with the number of larger aggregates kept as low as possible.

The standard growth conditions for (U)NCD used an Ar-rich gas mixture containing 1%CH_4 and a similar amount of H_2 to stabilise the plasma, giving a total gas flow $F_{total} = 520$ sccm. The substrate temperature, T_s, was measured using a 2-colour optical pyrometer, whilst the visible size and shape of the plasma ball could be viewed through a side-mounted quartz viewport, which was also used for optical emission spectroscopy (OES) measurements. A second chamber was used for the cavity ring down spectroscopy (CRDS) measurements [22]. This chamber was identical to the growth chamber except that it was fitted with tubular stainless steel side-arms which were coupled to the reactor by flexible knife-edge bellows assemblies and terminated with finely adjustable mounts that held high-reflectivity (>0.999) cavity end mirrors.

The Ar was then substituted in turn by the other inert gases (He, Ne and Kr, all 99.99% pure). The fraction of inert gas in the feedstock was varied between 93–98% while keeping F_{total} constant by decreasing the H_2 flow correspondingly and maintaining the CH_4 flow fixed at $F(CH_4) = 5$ sccm. Due to differences in the thermal conductivity and ionisation potential of the inert gases (see Table 1), the size, shape and temperature of the resulting plasma balls were different. For the same MW power and gas flow the visible size of the plasma ball decreased markedly on going from He to Kr. He-based plasmas were relatively

Table 2
Process conditions p, P, T_s and respective flow rates expressed as % of F_{total} identified as suitable for (U)NCD deposition with the different gas mixtures, plus the observed growth rate, G, and average crystallite size, <d>.

X	p /Torr	P /kW	T_s /K	F(X) /%	$F(H_2)$ /%	$F(CH_4)$ /%	G /(μm h^{-1})	<d> /nm
He	280–310	1.2–1.4	790–870	96.4–98.1	1.6–3.1	0.5	0.17	40–70
Ne	340–360	0.6–0.7	790–820	95.5–95.6	3.8	0.6–0.7	0.18	35–65
Ar	150–200	0.5–0.7	750–900	93.5–98.7	0.6–3.1	0.5–0.8	0.17–0.5	15–35
Kr	170	0.5	910–930	96.0–96.2	3.2	0.6–0.8	0.5–0.8	15–35

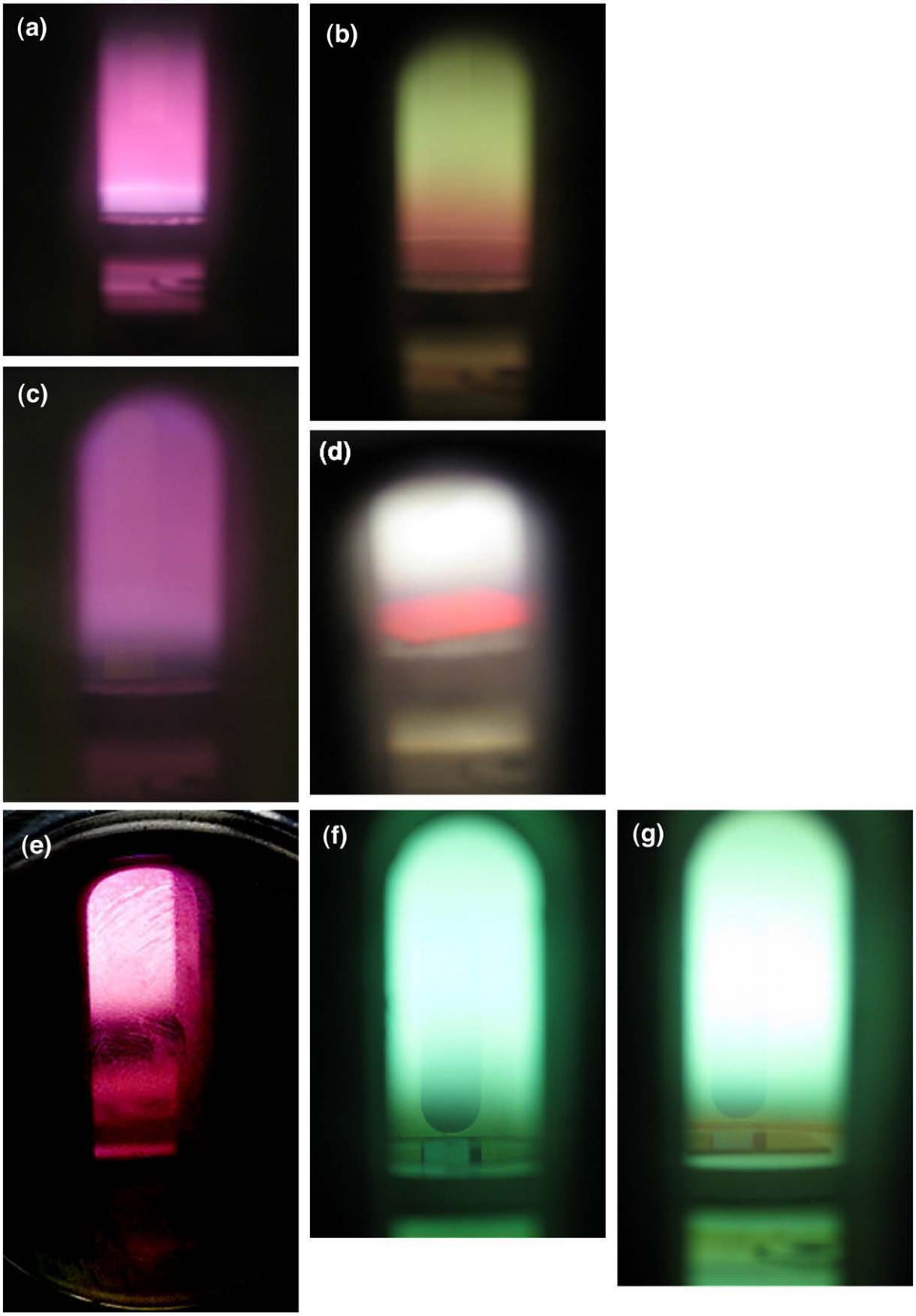

Fig. 1. Colour photographs of the plasmas taken through the viewport. The photos are of each of the inert gas plasmas, first with composition X/1%H_2 and then after adding 0.5% of CH_4, *i.e.* X/1%H_2/0.5%CH_4, with 1 kW microwave power at 175 Torr, 520 sccm total gas flow. (a) He/H_2, (b) He/H_2/CH_4, (c) Ne/H_2, (d) Ne/H_2/CH_4, (e) Ar/H_2, (f) Ar/H_2/CH_4, (g) Kr/H_2/CH_4. No photo of the Kr/H_2 plasma was taken due to its instability, however its colour was similar to that of Ar/H_2 in (e).

stable, and required little or no H_2 to be added to strike or maintain the discharge. Conversely, Kr-based plasmas required a few % H_2 to be added to initiate and maintain the discharge — otherwise they became unstable, readily forming unwanted small 'secondary plasmas' around the chamber, with the main plasma often jumping to the upper quartz window or extinguishing. The behaviour for Ne and Ar fell between these two cases.

As a result of the visibly different sizes (*i.e.* volume V_p) and therefore, presumably, power densities ($Q \sim P/V_p$, where P = MW power) of each inert gas plasma, the optimum deposition conditions for (U)NCD were also different in each case. To locate the process window for successful (U)NCD deposition, the input power P and gas pressure p were adjusted depending on the inert gas used, in order to achieve a similar substrate temperature. Table 2 shows the process windows inside which U(NCD) deposition was successful in producing continuous and uniform films of similar morphology. It should be noted that a greater number of films were grown using He- and Ar-rich plasmas and, as such, a broader range of process parameters investigated. The reported values should not be taken as limits outside which (U)NCD deposition is impossible, but rather as a set of parameters where the requisite films can be produced. U(NCD) deposition was not successful at $T_s < 750$ K, while $T_s > 1000$ K produced films with high sp^2 carbon or graphitic content.

2.2. Spectroscopic measurements of the plasma

The temperature of the gas, and therefore the substrate, was strongly dependent upon the chamber pressure, which determined the size of the plasma ball, and hence the power density of the plasma. As mentioned above, to achieve conditions for film growth, the pressure needed to be changed depending on the inert gas used. However, to compare the emission intensities from a variety of species for each inert gas plasma, a set of spectra were collected for a set of fixed conditions: $P = 1$ kW, $p = 175$ Torr, $F = 520$ sccm. A fibre optic light pipe was used to collect emission from the centre of the plasma ball, which was then dispersed and analysed using an Oriel Instaspec IV spectrometer. The column densities of H($n = 2$) atoms at $z = 9.8$ mm above the substrate were also probed by CRDS at 656 nm using a dye laser pumped by a Nd:YAG laser [22] under the same process conditions.

2.3. Film characterisation

The deposited films were analysed by scanning electron microscopy (SEM, JEOL JSM 6330F), atomic force microscopy (AFM, Veeco Multimode with Nanoscope V controller), and laser Raman spectroscopy at room temperature and with laser excitation wavelengths of both 325 nm (UV, HeCd) and 514 nm (green, Ar^+) using a Renishaw 2000 spectrometer.

3. Results and discussion

3.1. Plasma behaviour and appearance

The large increase in atomic mass and electron count down the group from He to Kr naturally led to differences in the plasmas used for CVD growth, as these two parameters determined the diffusion, collisional quenching and heating, electron excitation and heat transfer within the discharge. Visually, these effects manifested themselves via differences in the colour, size and brightness of the respective plasmas, as well as by controlling the intensity and appearance of emission spectra and the substrate temperature — which was an indirect measure of the plasma gas temperature (since the substrate heating in our system came entirely from the nearby plasma). Colour photographs of each of the plasmas can be seen in Fig. 1.

Helium has low mass but a relatively high thermal conductivity of 0.151 W m^{-1} K^{-1} at 300 K (rising to 0.566 W m^{-1} K^{-1} at 2000 K) [23]. He-based plasmas were more diffuse and cooler than those involving the other inert gases, with weak emission intensities for all observed species. Visually, they appeared to have a dull, pink colour which became greener with increasing CH_4 percentage. At the other end of the scale, Kr-based plasmas, with a thermal conductivity ~20 times lower than that of He, were smaller, but hotter, with intense emission from C_2 Swan bands appearing across the visible region of the spectrum, giving these plasmas a bright, green/white coloration. The behaviour of Ne and Ar fell between these two extremes.

The gas temperature was determined by fitting the rising baseline observed in optical emission spectroscopy to a black-body radiation equation [24]. The background emission in these H-poor plasmas has been attributed to small amounts of solid soot particles, especially near the cooler edges of the plasma. The soot particles achieve local thermal equilibrium with the gas, and black-body emission from these can be used to characterize the local gas temperature at the plasma edges [25]. For a set of standard conditions: $p = 175$ Torr, $P = 1$ kW and a plasma composition of 91%X/4%CH_4/5%H_2, the gas temperatures estimated by this method increased from 1950 K for He, through 2200 K for Ne, 2550 K for Ar, to 2600 K for Kr (with associated uncertainties of ± 100 K). This was accompanied by a proportionate increase in T_s from 800 K to 1120 K, respectively, when running the He and Kr plasmas under these conditions.

3.2. Growth rate and morphology of films

The crystallite size was estimated by inspecting SEM images such as those shown in Fig. 2 which show a small decrease in the average diameter working down the group from He to Kr. All films have an average crystallite size < 100 nm, with He-based plasmas producing crystallites of 40–70 nm, compared with 35–65 nm with Ne and 15–35 nm with Ar and Kr plasmas — approaching that for UNCD. In the two latter cases, longer range aggregation was observed with the crystallites lining up into 'cigar-shaped' forms. Similar aggregation has been observed by other groups [26,27], and these structures can also be observed in the AFM images in Fig. 3, although their formation mechanism remains unclear.

The growth rate was estimated by SEM cross-sectional analysis, and the results are seen in Table 2. The growth rates increased slightly with increasing mass of the inert gas, from a value of ~0.17 μm h^{-1} for He to ~0.5 μm h^{-1} for Kr, depending on the conditions used. This relative insensitivity to the identity of the inert gas probably arises because P and p were varied to achieve similar values of T_s (and therefore, by implication, of the near-substrate gas temperature) and it is likely that these are the dominant parameters controlling thermal dissociation of H_2. Subsequent adsorption and recombination of H atoms at the surface are the main sources of substrate heating,[28] and these reactions play a key role in determining the growth rate.

3.3. Raman analysis

The trend in crystallite size is supported by evidence from UV-Raman analysis, with spectra showing strong resonances for the sp^2-carbon-related D and G bands at 1360 and 1580 cm^{-1}, respectively, as well as smaller peaks at 1170 cm^{-1} (often called the 'UNCD peak') corresponding to *trans*-polyacetylene trapped at nanodiamond grain boundaries [29], and the sp^3 diamond peak at 1332 cm^{-1} [30], see Fig. 4. These four peaks can be fitted to Gaussian functions allowing peak ratios to be compared to give an indication of the proportion of sp^2 to sp^3 carbon in the film. As films with smaller crystallites will contain proportionately more grain boundary material, the diamond peak should decrease relative to the graphitic sp^2 peaks, and this trend is confirmed in Fig. 5. We observe a decrease in the height of the diamond peak relative to those of the G-band (a similar trend is seen when comparing the diamond and D-band features) from films grown using He to Kr plasmas. The ratio of the UNCD peak to the sp^3 diamond peak increases across the family of inert gases indicating an increase in grain boundary material. Such trends are fully consistent with the decrease in crystallite size in films grown from He- to Kr-rich plasmas revealed by electron microscopy.

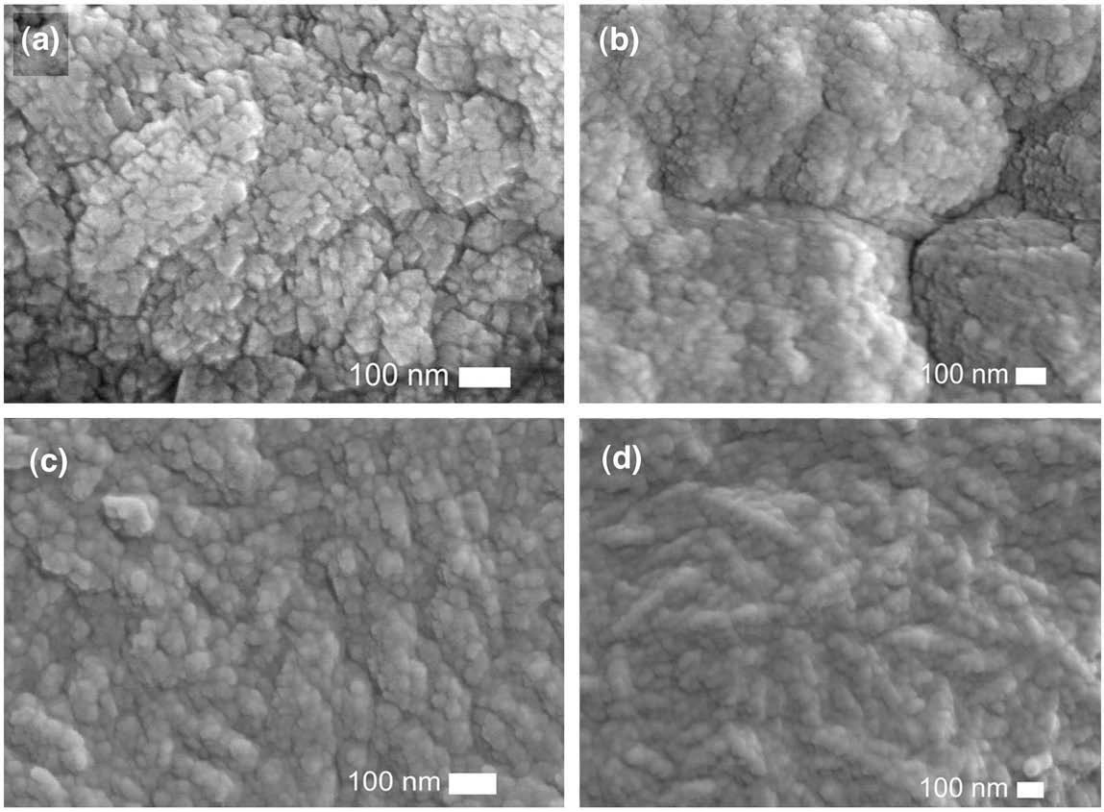

Fig. 2. High resolution SEM images showing surface morphology of (U)NCD films grown in the four inert gas mixtures: (a) He, (b) Ne, (c) Ar and (d) Kr using the process conditions described in Table 1.

3.4. OES and CRDS analysis of the plasma

Typical OES spectra from $Ar/CH_4/H_2$ and $Kr/CH_4/H_2$ plasmas under the standard MW power ($P = 1$ kW) and pressure ($p = 175$ Torr) conditions are shown in Fig. 6. When increasing $F(CH_4)$ from 0 to 20 sccm (while keeping F_{total} constant by reducing the H_2 flow accordingly), the OES data shown in Fig. 7 indicate different behaviours for each emitting species. The peak at 563 nm, which is representative of the $C_2(d^3\Pi_g - a^3\Pi_u\ \Delta v = +1)$ Swan band emission, shows a near linear increase with increasing CH_4 concentration, $[C_2] \sim F(CH_4)$, while the CH emission (at 431 nm) rises as $[CH] \sim (F(CH_4))^{0.5}$ and the C_3 band centred at 405 nm rises as $[C_3] \sim (F(CH_4))^{1.5}$.

The relative trends in CH and C_2 emission intensities with $F(CH_4)$ mirror those seen previously in H-rich hydrocarbon/H_2 plasmas [22,31]. As in that case, the present observations can be explained by recognising that, irrespective of the choice of source gas, C_2H_2 will be the dominant hydrocarbon in the plasma region, (except in the hot plasma central core with extremely high gas temperatures $T_g \sim 3200$ K for He and $T_g \sim 3550$ K for Ar) and that equilibration amongst and between the various C_1H_x and C_2H_y species ensure the respective near square root (for CH and other C_1H_x) and near linear (for C_2 and other C_2H_x) dependences on input carbon fraction [22]. Model calculations show that the dominant production/loss reactions for C_3 molecules in our plasma conditions are the reactions $C + C_2H_2 \leftrightarrow C_3 + H_2$, $C + C_2H \leftrightarrow C_3 + H$ and $C_2 + C_2 \leftrightarrow C_3 + C$. All these reactions are in equilibrium in the hot region providing the dependence $[C_3] \sim (F(CH_4))^{1.5}$ in agreement with the OES observations.

Cavity ring-down spectroscopy was used to probe the population in $H(n = 2)$ level for each of the inert gas plasma mixtures, over a somewhat wider range of $F(H_2)$ flow rates. Fig. 8 highlights similarities and differences in the $H(n > 1)$ versus $F(H_2)$ dependences from CRDS and OES measurements: He and Ne dominated gas mixtures show similar trends, with the $H(n > 1)$ densities decreasing

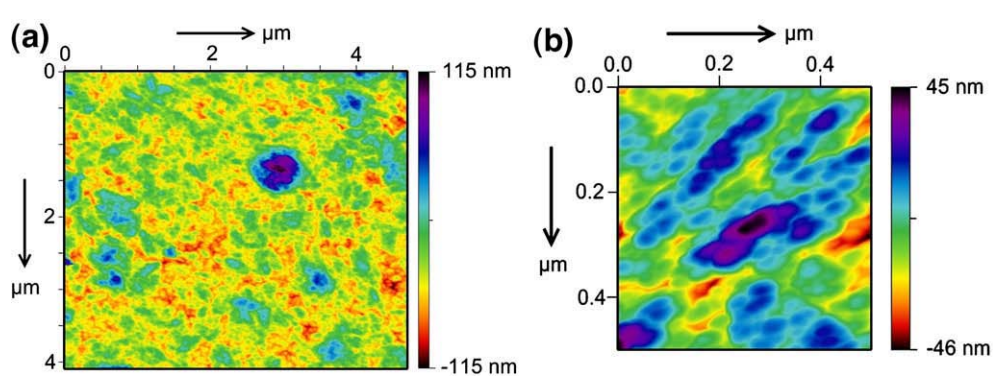

Fig. 3. AFM images of two films grown in an $Ar/H_2/CH_4$ plasma ($p = 170$ Torr, $P = 0.7$ kW, $T_s = 900$ K) over an area of (a) $4.7 \times 4.1\ \mu m^2$ (showing some larger aggregates as a result of the inhomogeneous nucleation layer) and (b) $0.5 \times 0.5\ \mu m^2$ (illustrating the alignment and/or elongation of individual nanodiamond crystals).

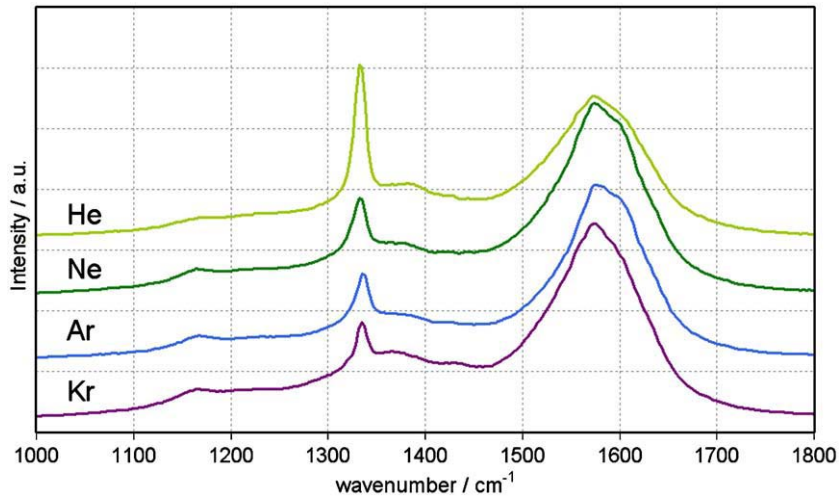

Fig. 4. Laser Raman spectra (325 nm excitation) from films grown in $X/CH_4/H_2$, where X = He, Ne, Ar, Kr under process conditions listed in Table 1. The main peaks are: Diamond (sp^3) 1332 cm^{-1}, *trans*-polyacetylene ('UNCD peak') 1170 cm^{-1}, sp^2 D-band 1360 cm^{-1} and sp^2 G-band 1580 cm^{-1}. The various spectra have been offset vertically for ease of display. For comparison, the Raman spectrum (not shown) from a film grown with 1%CH_4/H_2 gas mixtures but otherwise identical conditions consists of a flat baseline with a single, sharp, intense diamond peak at 1332 cm^{-1}. The 'UNCD' peak and D and G bands due to sp^2 carbon are no longer discernible.

with increasing $F(H_2)$ more steeply for He than Ne. When X = Ar the opposite behaviour is observed, with the $H(n>1)$ densities increasing with $F(H_2)$. Analysis of these data using 2D model calculation results will be reported in the next section.

3.5. Modelling of $Ar/CH_4/H_2$ and $He/CH_4/H_2$ plasmas

Given the cylindrical symmetry of the MW-CVD reactor chamber, 2-D modelling of the gas phase plasma chemistry and transport processes [12,14,15,31] can predict gas and electron temperatures, absolute concentrations of the various hydrocarbon molecules, radicals and ions under a range of process conditions, as a function of height (z) above the substrate centre and radial coordinate (r). This model of MW PECVD processes in H/C/Ar mixtures was applied and tested on various (UNCD [15], MCD [31] and SCD [14]) deposition regimes. The plasma chemistry model [31] for Ar/C/H mixtures includes ~290 forward and reverse reactions for neutral species (C, CH, $^3CH_2$, $^1CH_2$, CH_3, CH_4, $C_2(X)$, $C_2(a)$, C_2H, C_2H_2, C_2H_3, C_2H_4, C_2H_5, C_2H_6, C_3, C_3H, C_3H_2, C_4, C_4H, C_4H_2, H, $H_2(v=0,1,2)$, electronic excited levels $H(n=2)$, $H(n=3)$, H_2^*, Ar* (the lowest metastable levels) and Ar** (the lowest levels involved in resonance fluorescence)), and charged species (electrons, and the ions Ar^+, ArH^+, H^+, H_2^+, H_3^+, C^+, C_2^+, C_3^+, CH^+, C_2H^+, $C_2H_2^+$, $C_2H_3^+$, C_3H^+). The electron energy distribution function (EEDF), $n_e(\varepsilon)$, is calculated by solving the Boltzmann equation in a two-term approximation and the EEDF is used for calculations of the electron-particle reaction coefficients [31]. A similar plasma-chemical mechanism was developed for He/C/H mixtures.

Simulations were carried out for two 'base' experimental regimes for NCD deposition: $p=170$ Torr, $P=700$ W, $T_s=873$ K, $F_{total}=510$ sccm for a 0.5%CH_4/1%H_2/98.5%Ar mixture; and $p=300$ Torr, $P=1300$ W, $T_s=873$ K, $F_{total}=510$ sccm for a 0.5%CH_4/1%H_2/98.5%He mixture. The diameter d and height h of the cylindrical plasma region were taken from the OES observations: $d\sim9$ cm, $h\sim5$ cm and $d\sim7$ cm, $h\sim3.5$ cm for Ar and He dominated mixtures, respectively.

Peculiarities of the inert gases under investigation reveal themselves experimentally in the different behaviours of the H atom excited

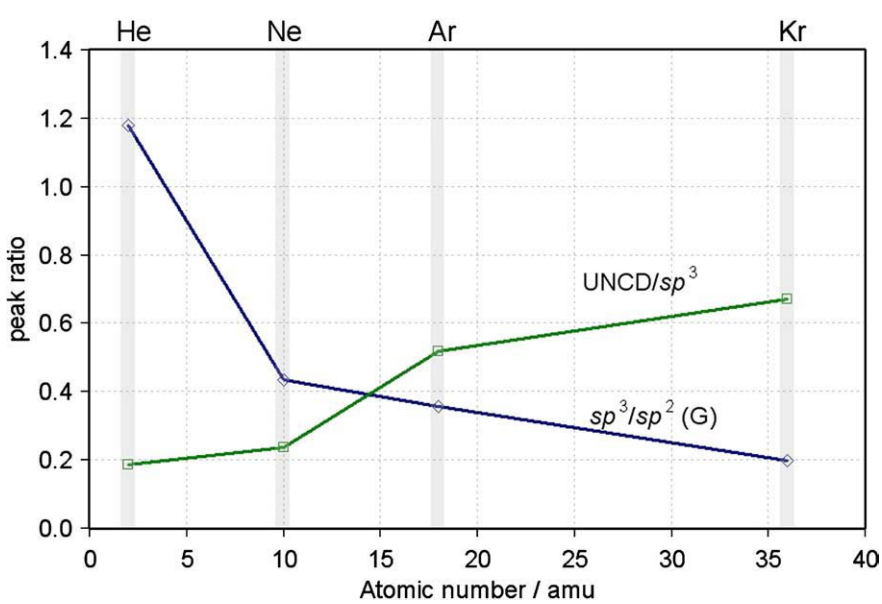

Fig. 5. Ratios of selected peak intensities in UV-Raman spectra of (U)NCD films grown with each inert gas plasma. The peaks are defined in the caption to Fig. 4.

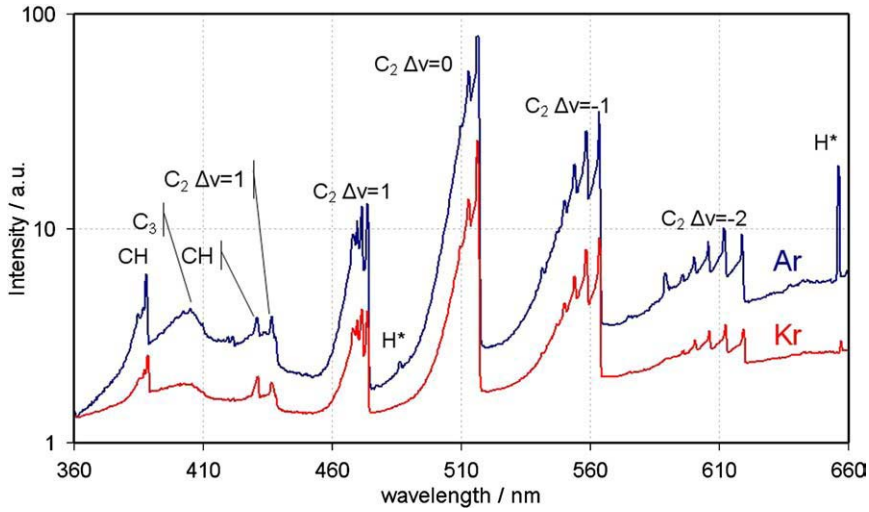

Fig. 6. Typical OES spectra from $Ar/CH_4/H_2$ and $Kr/CH_4/H_2$ plasmas operating under the standard MW power and pressure conditions given in Section 3.1 illustrating the reduction in H* intensity for the Kr-rich plasma. Note that the intensities are plotted on a logarithmic scale.

states (Fig. 8). The H(n>1) population is determined by electron impact excitation of H(n=1) atoms in the plasma: [H(n>1)]~k_n n_e·[H (n=1)]. The excited state populations thus depend (linearly) on the concentration of the latter, and on the electron characteristics (n_e and electron temperature T_e) [31]. More precisely, the excitation rate coefficient k_n depends on the high energy 'tail' of the EEDF — *i.e.* on electrons with energy ε>10 eV. As an approximation, we can express the excitation rate coefficient as a function of two temperatures, $k_n(T_e, T^*)$ [32], where T^* is the temperature of the EEDF 'tail'. In all cases, for a given level of power density $Q \sim P/V_p$, increasing $F(H_2)$ will result in an increase in the concentration of H(n=1) atoms and a decrease of T_e, but its effect upon T^* will be more variable. The decrease of T_e with $F(H_2)$ (and $F(CH_4)$) can be explained by electron energy losses in low threshold processes (*i.e.* vibrational and rotational excitations) that are specific to molecular gases. At the same time, T^*, which determines the ionization rate (and the rates of populating electronically excited states), cannot vary significantly given the electron densities required for absorption of the given input power. This latter conclusion is confirmed, indirectly, by the OES and CRDS measurements of the excited H atom concentrations, which for any given X do not vary greatly (*i.e.* by orders of magnitude) with variation in $F(H_2)$ (Fig. 8).

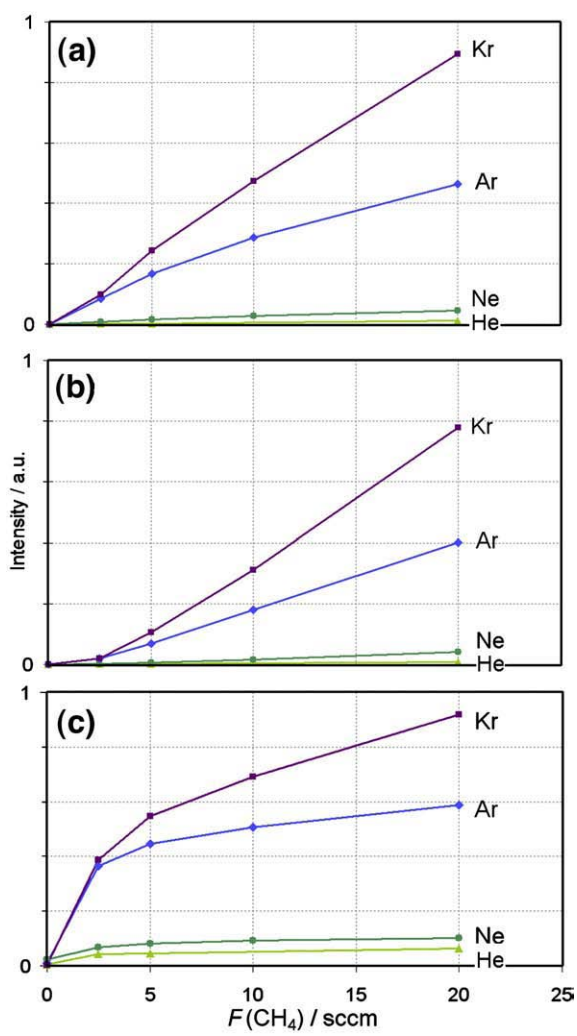

Fig. 7. Dependence of (a) C_2 (563 nm), (b) C_3 (405 nm) and (c) CH (431 nm) emissions on $F(CH_4)$ measured by OES for each inert gas plasma, using a 91%X/4%CH_4/5%H_2 gas mixture, with p=150 Torr and P=1 kW.

The calculated electron temperatures T_e and maximum gas temperatures T_{max} in the (U)NCD deposition regimes were: T_e~2.23 eV and T_{max}~3220 K for the 0.5%CH_4/1%H_2/He mixture, and T_e~2.74 eV and T_{max}~3550–3600 K for the 0.5%CH_4/1%H_2/Ar mixture. By way of comparison, values of T_e~1.28 eV and T_{max}~2926 K were calculated previously for the MCD deposition regime in this same reactor using a 4.4%CH_4/7%Ar/H_2 mixture at p=150 Torr and P=1.5 kW [31]. The plasma parameters in the He-rich (U)NCD mixture thus appear to resemble those of the hydrogen rich mixture more closely than do those of the Ar (and other heavier inert gas) based mixtures. Elastic collisions with the light He atoms (with associated energy loss $\Delta\varepsilon \sim 2m_e\varepsilon/M$, where m_e and M are the electron and atomic mass, respectively) are found to play an important role in the plasma energy balance, somewhat reminiscent of the role of H_2 rovibrational excitations in H_2 dominated mixtures. Integrated over the entire plasma volume, ~50% of the input power to the He dominated mixture is partitioned into such elastic losses. This fraction is spatially dependent, however, ranging from ~30% to ~70% in different regions. This is illustrated in Table 3, which shows the more important power absorption channels near the substrate and in the plasma centre, for both He and Ar dominated gas mixtures. From Table 3, we note significant spatial variations of power density Q even in the case of a uniform electron temperature T_e. Q is a minimum in the plasma centre (because of atomization and the paucity of molecular species in this hot region), but is maximal near the substrate (because of the efficient recovery of molecular species at the lower gas temperatures in this region and from recombination processes at the surface). Excitation

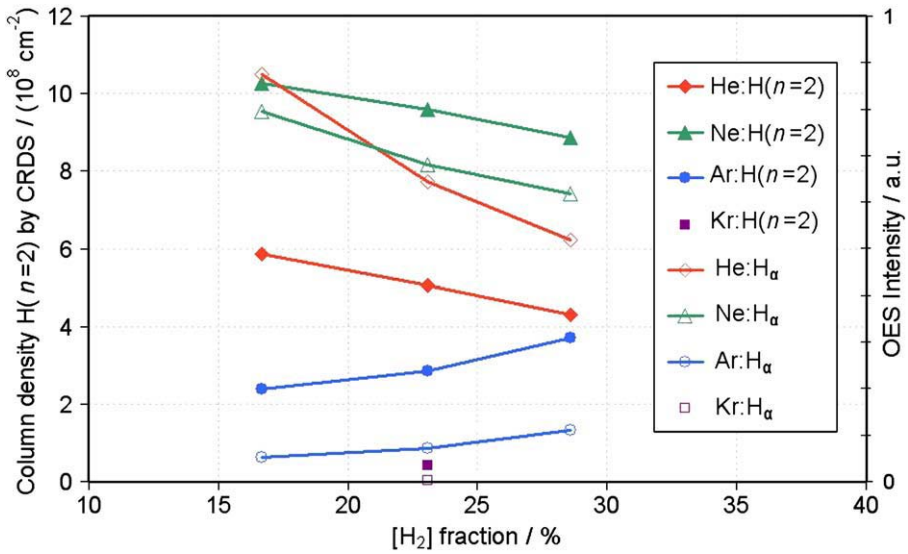

Fig. 8. Excited H atom densities in the plasma probed by two methods: (a) CRDS-measured H($n=2$) column density (filled symbols) and (b) OES-measured H_α 656 nm emission intensity (open symbols), as a function of H_2 fraction in the $X/H_2/CH_4$ plasma. Measurements were carried out at $P=1$ kW, $p=175$ Torr and with a higher H_2 fraction than used for (U)NCD film deposition conditions to prevent excessive heating of the top quartz window in the MW reactor.

of Ar and H atoms, and their further participation in Penning and/or associative ionization reactions, are important contributors to the total ionization rate. The modeling allows estimation of the way in which the input power is partitioned into gas heating (directly, as elastic losses and, indirectly, as a result of rotational and vibrational relaxation), radiation losses, and plasma-chemical activation of the H/C process gas mixture. This partitioning (integrated over the plasma volume) is calculated to be ~88.5%, ~5.1% and 6.4%, respectively, for the He-rich mixture, and ~61.3%, ~25% and 13.7%, respectively, for the Ar-based mixture. Thus, despite the different input powers in the two cases (1.3 kW versus 700 W for the He- and Ar-based mixtures), the power expended on plasma-chemical activation of the CH_4/H_2 process gas is similar for both of the optimized (U)NCD deposition regimes (*i.e.* ~83 W in He and ~96 W in the Ar-based mixture).

Table 3
Calculated absorbed percentage power fractions from stated local power density Q both at $z=0.5$ mm above the centre of the substrate and at the plasma centre, derived from 2-D modelling of: an $Ar/0.5\%CH_4/1\%H_2$ plasma operating at $p=170$ Torr, $P=700$ W; and a $He/0.5\%CH_4/1\%H_2$ plasma operating at $p=300$ Torr, $P=1.3$ kW. $F_{total}=510$ sccm and $T_s=873$ K in both cases. For H_2, n is the principal quantum number, while J and v refer to the rotational and vibrational quantum numbers, respectively.

Location	Near substrate, $z=0.5$ mm		Plasma centre	
Inert gas, X	Ar	He	Ar	He
Local power density, $Q/(W\ cm^{-3})$	9.3	20	0.73	2.8
	Absorbed power fraction (%)			
Process				
X + e, elastic losses	4.86	36.6	10.9	65.7
H + e, elastic losses	0.886	0.352	21.1	70.2
H_2 + e, elastic losses	3.21	2.74	0.494	0.776
$H_2(J)+e \leftrightarrow H_2(J+2)+e$	26.0	13.7	3.81	3.70
$H_2(v)+e \leftrightarrow H_2(v+1)+e$	43.3	38.1	5.76	9.59
$H+e \rightarrow H(n=2)+e$	0.791	0.278	27.0	8.76
$H_2+e \rightarrow H_2^*+e$	0.102	0.673	0.024	0.322
$X+e \rightarrow X^*+e$	4.51	0.014	15.4	0.0643
$X+e \rightarrow X^{**}+e$	3.02	0.0001	10.3	0.00054
$H_2+e \rightarrow H+H+e$	3.76	2.43	0.798	1.06
$C_2H_2+e \rightarrow C_2H+H+e$	7.36	3.02	0.0963	0.322
$H+e \rightarrow H^++e+e$	0.00051	0.0067	0.0022	0.256
$H_2+e \rightarrow H_2^++e+e$	7.53×10^{-6}	0.0316	0.00032	0.0188
$C_2H_2+e \rightarrow C_2H_2^++e+e$	0.064	0.392	0.0012	0.0622
$C_3+e \rightarrow C_3^++e+e$	0.0143	0.0221	0.077	0.263

The electronic structure, ionization and excitation thresholds, and electron collision cross-sections of the inert gas atoms also have an effect on the EEDF and the plasma chemistry in a $CH_4/H_2/X$ mixture. This can be seen from the variations in the dominant ionization channels shown in Table 3. The existence (or absence) of excited levels of X near, or below, the excited level of the species under study can influence their respective populations, as a result of collision induced changes to the EEDF in this energy range, and/or possible resonant exchange reactions with the inert gas atoms. The excited states of the inert gas atoms are located in the energy ranges 19.82–24.6 eV for He, 16.62–21.56 eV (Ne), 11.55–15.76 eV (Ar) and 9.9–14 eV (Kr). Thus, only Kr atoms have excited levels in close resonance with the H($n=2$) and H($n=3$) states (10.2 eV and 12.1 eV, respectively). In most respects the OES spectrum obtained from the Kr-based plasma is similar to that from the Ar-based plasma, apart from the observation that the H atom Balmer series — which is relatively intense for X/H_2 and $X/H_2/CH_4$ (X = He, Ne, Ar) plasmas — is absent for a Kr/H_2 plasma, and only present very weakly after methane is added (see Fig. 6). The results shown in Fig. 8 correlate well with the CRDS data, showing a marked decrease in H($n=2$) column density from He to Kr. The reduction in H($n=2$) and H($n=3$) concentrations for the

Table 4
Calculated gas temperature T_g and species concentrations at $z=0.5$ mm above the centre of the substrate derived from 2-D modelling of a $Ar/0.5\%CH_4/1\%H_2$ plasma and $He/0.5\%CH_4/1\%H_2$ plasma under the base conditions specified in the caption to Table 3.

X	Ar	He
T_g/K	1306	1193
Species	Number density/cm^{-3}	
X	1.23×10^{18}	2.38×10^{18}
H	3.42×10^{15}	2.57×10^{15}
H_2	1.99×10^{16}	4.03×10^{16}
CH_4	2.07×10^{11}	1.52×10^{13}
CH_3	1.27×10^{11}	3.06×10^{12}
CH_2	2.35×10^{9}	1.75×10^{10}
CH	1.54×10^{9}	3.32×10^{9}
C	4.69×10^{11}	1.11×10^{11}
C_2	1.21×10^{11}	1.25×10^{10}
C_2H	1.39×10^{12}	6.04×10^{11}
C_2H_2	2.17×10^{15}	5.43×10^{15}
C_3	4.39×10^{14}	2.95×10^{14}
C_3H_2	8.94×10^{13}	2.88×10^{14}
C_4H_2	1.26×10^{14}	2.44×10^{14}

Kr plasma is likely to be exacerbated by near resonant energy transfer reactions between excited H atoms and ground state Kr, *i.e.*

$$\mathrm{H}(n=2)+\mathrm{Kr}(4p^6)\rightarrow\mathrm{H}(n=1)+\mathrm{Kr}(4p^5 5s^1),\Delta E=-0.17\mathrm{eV}$$

$$\mathrm{H}(n=3)+\mathrm{Kr}(4p^6)\rightarrow\mathrm{H}(n=1)+\mathrm{Kr}(4p^5 5p^1),\Delta E=0.01\mathrm{eV}$$

and so on for H(n>3). The NIST Atomic Spectra Database [33] lists several excited states of Kr arising from the $4p^5 5s^1$ and $4p^5 5p^1$ configurations, and the energy mismatch (ΔE) values quoted above are for the closest resonance in each case. The net effect of such near resonances will be to provide an efficient route (not available to the lighter rare gases) for depopulating the excited states of H.

Table 4 lists the calculated gas temperature and number densities of many of the more abundant species at $z=0.5$ mm above the substrate centre for Ar/0.5%CH_4/1%H_2 and He/0.5%CH_4/1%H_2 plasmas operating at the base pressure and power conditions specified previously. Recent discussions of (U)NCD growth have tended to focus on C atoms and CH_3 radicals as likely growth species, but the predicted growth rates due to these species (using equations given in [15]) are only $G_C=0.033$ and $G_{CH3}=0.001$ μm h^{-1} for the Ar-based mixture and $G_C=0.001$ and $G_{CH3}=0.03$ μm h^{-1} for the He-based mixture. The switch in predicted growth species (from CH_3 dominated growth in the He plasma, to C for Ar) is noteworthy, but should be viewed with caution since both total growth rates are nearly an order of magnitude smaller than those observed experimentally (~0.15–0.5 μm h^{-1}). The reason for this discrepancy is unclear at present. Uncertainties include the possible contributions from C_3 (and higher) species — which are predicted to be more abundant in inert gas rich plasmas — though we concede that the lack of reliable reaction rate data at high temperatures may cause the model to overestimate the transformation of C_1 species into C_3H_x and C_4H_x species. As commented earlier, C_2 has also been mooted as a possible (U)NCD growth species, and the density of C_2 radicals in the (cooler) near-substrate region is indeed enhanced by plasma-chemical sources, but these densities are still substantially lower than the sum of $C+CH_3$ densities in all calculated regimes.

4. Conclusions

Despite slight differences in the plasma conditions and behaviour, all of the inert gas plasmas produced morphologically uniform and homogenous (U)NCD films at roughly the same growth rate, so long as the temperature of the gas and, therefore, the substrate, was high enough (T_s>750 K). SEM and Raman analysis shows a small decrease in grain size from 40–70 nm for He to 15–35 nm for Kr and a slight change in localized morphology, both of which may reflect changes in reactor conditions and the specifics of the particular inert gas. By combining and comparing experimental and theoretical studies of MW PECVD reactor processes, we have been able to identify inert-gas dependent peculiarities and their possible effects on the plasma chemistry, plasma parameters and film properties. The 2D modelling shows that ~50% of the input power in the base 0.5%CH_4/1%H_2/He gas mixture is dissipated via elastic collisions between electrons and He atoms, whereas such collisions only account for ~7% of the power consumed with a similar Ar-based plasma. Despite the different input powers for the optimized (U)NCD deposition regimes (1.3 kW for He, *cf* 700 W for the Ar based mixture), the power expended on plasma-chemical activation of the CH_4/H_2 process gas is similar for both mixtures (~83 W for He and ~96 W for Ar mixtures). The present calculations suggest a greater role for CH_3 radicals in growth from He-based plasmas (*cf* growth from C atoms in the case of the Ar-rich plasma), but underestimate the total growth rate by nearly an order of magnitude — hinting at a need for further consideration of possible contributions to growth from the more abundant C_3 (and other heavier) species. For optimum performance, small, controllable plasmas with high power density are required and, for this, the heavier the inert gas the better. Kr is the obvious candidate, however, its high cost, plus its tendency to form unstable plasmas, means that Ar remains the best choice for the inert gas when depositing (U)NCD films.

Acknowledgements

The authors would like to thank Dr. James Smith and Keith Rosser for technical and instrument support, Element Six Ltd for the long term loan of the MW reactors used in this work, and EPSRC and the Royal Society Wolfson Laboratory Refurbishment Scheme for funding. YuAM is grateful to RF Government for Key Science Schools grant No. 133.2008.2.

References

[1] P.W. May, Philos. Trans. R. Soc. Lond., A 358 (2000) 473.
[2] P.W. May, Science 319 (2008) 1490.
[3] S.J. Harris, Appl. Phys. Lett. 56 (1990) 2298.
[4] D.G. Goodwin, J.E. Butler, in: M.A. Prelas, G. Popovici, L.K. Bigelow (Eds.), chapter 11 in Handbook of industrial diamonds and diamond films, Marcel Dekker, New York, 1997.
[5] M.H. Nazaré, A.J. Neves (Eds.), Properties, Growth and Applications of Diamond, INSPEC, EMIS datareviews 26, Institute of Engineering and Technology, 2000.
[6] D.M. Gruen, O.A. Shenderova, A.Ya. Vul' (Eds.), Synthesis, Properties and Applications of Ultrananocrystalline Diamond, NATO Science Series part II, vol. 192, Springer, 2005.
[7] P.W. May, W.J. Ludlow, M. Hannaway, P.J. Heard, J.A. Smith, K.N. Rosser, Diamond Relat. Mater. 17 (2008) 105.
[8] X. Xiao, J. Birrell, J.E. Gerbi, O. Auciello, J.A. Carlisle, J. Appl. Phys. 96 (2004) 2232.
[9] W. Kulisch, C. Popov, Phys. Stat. Sol. (a) 203 (2006) 203.
[10] D. Zhou, T.G. McCauley, L.C. Qin, A.R. Krauss, D.M. Gruen, J. Appl. Phys. 83 (1998) 540.
[11] P.W. May, J.N. Harvey, J.A. Smith, Yu. A. Mankelevich, J. Appl. Phys. 99 (2006) 104907.
[12] P.W. May, Yu. A. Mankelevich, J. Appl. Phys. 100 (2006) 024301.
[13] P.W. May, Yu. A. Mankelevich, Mater. Res. Soc. Symp. Proc. PV-956 (2006) 0956-J07-04.
[14] Yu. A. Mankelevich, P.W. May, Diamond Relat. Mater. 17 (2008) 1021.
[15] P.W. May, Yu. A. Mankelevich, J. Phys. Chem. C 112 (2008) 12432.
[16] J. Birrell, J.E. Gerbi, O. Auciello, J.M. Gibson, J. Johnson, J.A. Carlisle, Diamond Relat. Mater. 14 (2005) 86.
[17] D. Zhou, D.M. Gruen, L.C. Qin, T.G. McCauley, A.R. Krauss, J. Appl. Phys. 84 (1998) 1981.
[18] J. Birrell, J.E. Gerbi, O. Auciello, J.A. Carlisle, J. Phys., Condens. Matter 18 (2006) S1771.
[19] J.R. Rabeau, P. John, J.I.B. Wilson, Y. Fan, J. Appl. Phys. 96 (2004) 6724.
[20] P. Tosi, D. Bassi, B. Brunetti, F. Vecchiocattivi, Int. J. Mass Spectrom. Ion Process. 145/150 (1995) 345.
[21] J. Griffin, P.C. Ray, Nanotechnology 17 (2006) 1225.
[22] J. Ma, J.C. Richley, M.N.R. Ashfold, Yu.A. Mankelevich, J. Appl. Phys. 104 (2008) 103305.
[23] C.Y. Ho, R.W. Powell, P.E. Liley, J. Phys. Chem. Ref. Data 1 (1973) 298.
[24] M.A. Elliott, P.W. May, J. Petherbridge, S.M. Leeds, M.N.R. Ashfold, W.N. Wang, Diamond Relat. Mater. 9 (2000) 311.
[25] K. Hassouni, F. Mohasseb, F. Bénédic, G. Lombardi, A. Gicquel, Pure Appl. Chem. 78 (2006) 1127.
[26] O.A. Williams, M. Nesládek, Phys. Status Solidi (a) 203 (2006) 3375.
[27] O.A. Williams, M. Nesládek, M. Daenen, S. Michaelson, A. Hofmann, E. Osawa, K. Haenen, R.B. Jackman, Diamond Relat. Mater. 17 (2008) 1080.
[28] W.A. Yarbrough, K. Tankala, M. Mecray, T. DebRoy, Appl. Phys. Lett. 60 (1992) 2068.
[29] A.C. Ferrari, J. Robertson, Phys. Rev. B 63 (2001) 121405.
[30] S. Prawer, R.J. Nemanich, Philos. Trans. R. Soc. Lond., A 362 (2004) 2537.
[31] J. Ma, M.N.R. Ashfold, Yu.A. Mankelevich, J. Appl. Phys. 104 (2008) 113304.
[32] J.I.A. Shkurenkov, Yu. A. Mankelevich, T.V. Rakhimova, Plasma Phys. Rep. 34 (2008) 780.
[33] http://physics.nist.gov/cgi-bin/AtData/main_asd.
[34] S.-C. Hwang, R.D. Lein, D.A. Morgan, Noble Gases, Kirk Othmer Encyclopedia of Chemical Technology, Wiley, 2005, p. 343.